In situ hydrolysis of a carbophosphazene ligand leads to one-dimensional lanthanide coordination polymers. Synthesis, structure and dynamic magnetic studies

Naushad Ahmed, Prem Prakash Sahu, Amit Chakraborty, Jessica Flores Gonzalez, Junaid Ali, Pankaj Kalita, Fabrice Pointillart, Saurabh Kumar Singh, Vadapalli Chandrasekhar

In situ Hydrolysis of a Carbophosphazene Ligand Leads to One-Dimensional Lanthanide Coordination Polymers. Synthesis, Structure and Dynamic Magnetic Studies[$]

Naushad Ahmed,[a ‡] Prem Prakash Sahu,[b, §] Amit Chakraborty, [a] Jessica Flores Gonzalez, [c §] Junaid Ali, [a] Pankaj Kalita,[a] Fabrice Pointillart,* [c] Saurabh Kumar Singh* [b] Vadapalli Chandrasekhar * [a]

[a] Tata Institute of Fundamental Research Hyderabad, Gopanpally, Hyderabad-500046, Telangana, India

[b] Department of Chemistry, Indian Institute of Technology Hyderabad, Kandi, Telangana-502285, India

[c] Univ Rennes, CNRS, ISCR (Institut des Sciences Chimiques de Rennes) - UMR 6226, 35000 Rennes, France

[‡] Current address: Department of Chemistry, Texas A&M University, College Station, Texas 77842, USA

[§] Authors contributed equally

[$] This manuscript is dedicated to Prof. R. Murugavel on his 60th birthday.

Abstract

An *in situ* hydrolysis of the P-Cl bonds of the carbophosphazene [{$NC(NMe_2)$}$_2${$NPCl_2$}] ($\mathbf{L}^{PCl2}$) in the presence of hydrated lanthanide(III) nitrates in a dichloromethane and methanol (2:1) solvent mixture afforded a series of novel 1D coordination polymers: [{$Ln(\mathbf{L}^{HPO2})_3(NO_3)_2(CH_3OH)(H_2O)$} $(Cl)]_n$ {where Ln(III) = Gd (**1**), Tb(**2**), Dy(**3**), or Er(**4**) and $\mathbf{L}^{HPO2}$ is the hydrolyzed carbophosphazene ($\mathbf{L}^{PCl2}$) ligand}. X-ray crystallographic analysis revealed that complexes **1**-**4** are isostructural and crystallized in the monoclinic crystal system having $P2_1/c$ space group. The coordination polymers are formed because of the involvement of the geminal P(O)(OH) moieties of the carbophosphazene ligand. Each lanthanide (III) ion is 9-coordinate (9O) in a distorted muffin geometry. Magnetic measurements revealed that both Dy^{III} and Er^{III} analogues exhibit field-induced single-molecule magnet (SMM) behavior at 0.8 kOe and 2.2 k Oe, respectively. At such dc fields, the dynamic magnetic susceptibility displays complex behavior with a triple magnetic relaxation contribution for **3,** while two contributions were identified for **4**. The observed static and dynamic magnetic behavior for complexes **1**-**4** were further rationalized with the aid of BS-DFT and CASSCF/SO-RASSI/SINGLE_ANISO calculations.

Introduction

Cyclophosphazenes are among the most widely studied inorganic heterocyclic ring systems. [1-5] This interest stems from many reasons. [6, 7] One, the rich diversity of stereo- and regioselective patterns observed in the nucleophilic substitution reactions of the six- and eight-membered rings such as $N_3P_3Cl_6$ and $N_4P_4Cl_8$ have been a topic of considerable attention. [8, 9] Two, the polymerization of $N_3P_3Cl_6$ to $[NPCl_2]_n$ and the subsequent macromolecular substitution of the P-Cl bonds by nucleophiles, has been a principal synthetic route for a large family of polyphosphazenes. [10, 11] Indeed, the latter is the most prominent family of inorganic polymers. A third reason of interest has been the utility of the cyclophosphazene motifs as support for the construction of multi-site coordination ligands. [6, 7] We and others have actively delineated this aspect of the cyclophosphazene chemistry in some detail.[8-9] Closely related to cyclophosphazenes are cyclocarbophosphazenes which can be considered as hybrids between the former and the organic heterocyles, s-triazines.[12, 13] Thus, cyclocarbophosphazenes have one or two carbon atoms in the skeletal ring in place of phosphorus. We have been engaged in developing the coordination chemistry of cyclocarbophosphazenes.[14, 15] Thus, for example, we have observed that selective P-N bond hydrolysis occurs in the interaction of $[\{NP(3,5\text{-}Me_2Pz)_2\}\{NC(3,5\text{-}Me_2Pz)\}_2]$ with various metal ions leading to the formation of ensembles of variable nuclearity. [16] On the other hand, we were also able to demonstrate hydrolytic stability in ligands such as the guanidine derivative, $[\{NCCl\}_2\{NP(NC(NMe_2)_2)_2\}]$, the hydrazone ligands, $[\{NC(N(CH_3)_2)\}_2\{NP\{N(CH_3)N{=}CH\text{-}C_6H_3\text{-}(o\text{-}OH)(m\text{-}OCH_3)\}_2\}]$ and $[\{N_2P_2(O_2C_{12}H_8)_2\}\{NP\{N(CH_3)N{=}CH\text{-}C_6H_3\text{-}(o\text{-}OH)(m\text{-}OCH_3)\}_2\}]$, or the pyridyloxy ligands, $[NC(NMe_2)]_2[NP(p\text{-}OC_5H_4N)2]$ and $[NC(NMe_2)]_2[NP(m\text{-}OC_5H_4N)_2]$.[15, 17] In view of this we were

curious to investigate the coordination behavior of [{NC(NMe$_2$)}$_2${NPCl$_2$}] (**L**^{PCl2}) towards hydrated metal salts with a view to examine if the P-Cl bond could be hydrolyzed and if the *in situ* generated P(O) motifs could be engaged in coordination leading to a coordination polymer chain. In view of our extensive interest in lanthanide ion complexes as molecular magnets such as single-molecule magnets (SMMs)[18-20] and single-ion magnets (SIMs)[21-23] we chose to examine the reactivity of (**L**^{PCl2}) with hydrated lanthanide nitrates. Accordingly, herein, we report the synthesis, structure and magnetic studies of the 1D coordination polymers, [{Ln(**L**^{HPO2})$_3$(NO$_3$)$_2$(CH$_3$OH)(H$_2$O)}(Cl)]$_n$ { Ln(III) = Gd (**1**), Tb (**2**), Dy (**3**), or Er (**4**). While the Dy^{III} analogue exhibits zero-field out-of-phase magnetic susceptibility signals, which could be well resolved on the application of a moderate dc magnetic field, the Er^{III} analogue revealed a slow magnetic relaxation behavior observed under 2.2 kOe applied magnetic field. We carried out BS-DFT and CASSCF/SO-RASSI/SINGLE_ANISO calculations to understand and rationalize the observed magnetic behavior.

Experimental

Chemicals and solvents purchased from commercially available sources (Sigma Aldrich and Alfa Aesar) were used without further purification. All the reactions were performed under aerobic conditions unless otherwise mentioned. The carbophosphazene ligand [{NC(NMe$_2$)}$_2${NPCl$_2$}] (**L**^{PCl2}) was synthesized according to literature procedure.[14, 16, 17] Solid state FT-IR spectra were recorded using KBr pellets on a Perkin-Elmer FT-IR spectrometer in the 400 to 4000 cm^{-1} range. Thermogravimetric analyses (TGA) were carried out by using a TGA 550 TA instruments, under an atmosphere of dinitrogen, at a heating rate of 10 °C per minute. The dc magnetic susceptibility measurements were performed on immobilized solid polycrystalline sample with a Quantum Design MPMS-XL SQUID magnetometer between 2 and 300 K in an applied magnetic field of

0.02 T for temperatures of 2-20 K, 0.2 T for temperatures of 20-80 K and 1T for temperatures of 80-300 K. The ac magnetic susceptibility measurements were performed on a Quantum Design MPMS-XL SQUID for frequencies between 0.1 and 1000 Hz and a Quantum Design PPMS magnetometers for frequencies between 100 and 10000 Hz. These measurements were all corrected for the diamagnetic contribution as calculated with Pascal's constants. To prevent desolvation of the samples, they have been introduced at 150 K under a flux of helium in both SQUID and PPMS magnetometers. It may be mentioned that the thermal gravimetric analysis (TGA) data (Figure S17, ESI) indicates that when the temperature reaches 70°C, the sample experiences a weight loss of around 8.5%, equivalent to the departure of two methanol molecules from the crystal lattice. This indicates that the compound is quite stable and does not lose solvent during the temperatures where the magnetic measurements were carried out.

Synthesis of 1-4

$[\{Gd(L^{HPO2})_3(NO_3)_2(CH_3OH)(H_2O)\}(Cl)]_n$ (1)

The carbophosphazene $\mathbf{L}^{PCl2}$ (0.2 g, 0.7812 mmol) was dissolved in 30 mL of dichloromethane/methanol solvent mixture (2:1) and then $Gd(NO_3)_3 \cdot 6H_2O$ (0.117 g, 0.2604 mmol) salt was added to this solution. The reaction mixture was stirred for two hours at room temperature and then filtered. Colorless block-shaped crystals of **1** suitable for X-ray diffraction were isolated from the filtrate within 24 hours by the slow evaporation of the solvents. Yield 0.135 g, 35% (based on Gd), FT-IR (Figure S16): $\upsilon_{\text{-OH}} = 3390\ cm^{-1}$; $\upsilon_{\text{-P-OH}} = 3192\ cm^{-1}$; $\upsilon_{\text{-C=N}} = 1626\ cm^{-1}$; $\upsilon_{\text{-P=O}} = 1101\ cm^{-1}$. Elemental analysis: Cal. C, 26.09; H, 6.01; N, 17.52, Found: C, 26.30; H, 5.95; N, 17.59.

[{Ln(L^{HPO2})$_3$(NO_3)$_2$(CH_3OH)(H_2O)} (Cl)]$_n$ (Ln = Tb^{III} (2); Dy^{III} (3); Er^{III} (4)). A similar procedure as used for the preparation of **1** was used to prepare **2**-**4**. The details are given below.

2: Yield 0.160 g, 46% (based on Tb), FT-IR (Figure S16): υ_{-OH} = 3380 cm^{-1}; υ_{-P-OH} = 3182 cm^{-1}; $\upsilon_{-C=N}$ = 1622 cm^{-1}; $\upsilon_{-P=O}$ = 1097 cm^{-1}. Elemental analysis: Cal. C, 26.37; H, 6.01; N, 17.57. Found: C, 26.58; H, 6.29; N, 17.80.

3: Yield 0.145 g, 39% (based on Dy), FT-IR (Figure S16): υ_{-OH} = 3372 cm^{-1}; υ_{-P-OH} = 3180 cm^{-1}; $\upsilon_{-C=N}$ = 1620 cm^{-1}; $\upsilon_{-P=O}$ = 1093 cm^{-1}. Elemental analysis: Cal. C, 26.30; H, 5.99; N, 17.52. Found: C, 26.05; H, 5.50; N, 17.34.

4: Yield 0.150 g, 43% (based on Er), FT-IR (Figure S16): υ_{-OH} = 3382 cm^{-1}; υ_{-P-OH} = 3170 cm^{-1}; $\upsilon_{-C=N}$ = 1630 cm^{-1}; $\upsilon_{-P=O}$ = 1104 cm^{-1}. Elemental analysis: Cal. C, 26.20; H, 5.97; N, 17.46. Found: C, 26.06; H, 5.70; N, 17.30.

X-ray crystallography

For the single crystal X-ray data collection, we have used the Rigaku Xtal LAB X-ray diffractometer (MoK_α, λ = 0.71073 Å) instrument at 297 K temperature. The data integration (with narrow frame algorithm) and empirical absorption correction (SCALE3 ABSPACK scaling algorithm program) were performed using $CrysAlis^{Pro}$ software. For structural solution and elucidation Olex-2 software[24] was used. The direct methods in SHELXTL used to solve the structure and refinement by the full matrix least-squares method on F^2 (SHELXL-2014).[25, 26] (CCDC 2296556-2296559). Data for compounds 2-4 were collected multiple times. Due to poor crystal quality, we observed a low data completeness: 84.7% for compound **2**, 89% for compound **3**, and 89.2% for compound **4**. However, all other crystallographic parameters are in the acceptable

limits. There were few disordered solvents in the crystals, these solvents were squeezed using the solvent mask. The relevant information regarding the masked solvents is appended in the respective CIF files.

Computational Methodology

For the calculation of the single-ion anisotropy and spin-Hamiltonian parameters (SH) of the individual paramagnetic ions (Tb^{III}, $Dy^{III,}$ and Er^{III}) in **2-4**, we have carried complete active space self-consistent field (CASSCF) calculations[27] using MOLCAS 8.2 code.[28] All the calculations were performed on the X-ray crystal structures where the position of hydrogens was optimized at BP86[29, 30] level of theory and def2-SVP basis set.[31, 32] For calculations of SH parameters in the CASSCF framework, the active space is comprised of the CAS (n,7) (where n = 8, 9, and 11, representing the number of active electrons in the seven 4*f*-based active orbitals of Tb^{III}, Dy^{III} and Er^{III}. We have employed the basis set from the ANO-RCC library (see Table S9 for detailed basis set contraction scheme).[33 34] The Dy(III) ion has $4f^9$ configuration and possesses a $^6H_{15/2}$ ground state and using an active space of CAS(9,7), we have computed 21 spin-free sextet states. Here, we have not calculated other higher excited states for the Dy^{III} ion, as the 21 roots are significant enough to describe the magnetic properties.[35-39] This methodology has been very robust in computing the magnetic properties of lanthanide complexes.[40-44] For Tb^{III} ion, with an active space of CAS (8,7) we have computed seven septets and 140 quintet spin-free states. On the other hand, for Er^{III} ion, we have computed 35 quartets and 112 doublet states using an active space of CAS(11,7). The computed spin-free states for each Ln^{III} centre were subsequently mixed using a spin-orbit restricted active space spin-interaction (SO-RASSI) to calculate the spin-orbit states.[45] These computed spin-orbit states were taken to the SINGLE_ANISO module[46] to extract the g-

values, crystal field parameters, ab initio blockade barrier and *d.c.* magnetic properties (magnetic susceptibility and magnetization). Resolution of identity Cholesky decomposition (RICD)[47] was turned on to save the disk space. The computed relative energies of the spin-free states, spin-orbit states, and the g-values for all Ln^{III} ions are provided in the Supporting Information.

Scalar relativistic density functional theory (SR-DFT) calculations were performed to compute the isotropic magnetic exchange interaction between the Gd^{III} centers in **1**, using the ORCA 4.2.1 code.[48, 49] Calculations were performed using the B3LYP[50] level of theory on the dimeric model complex extracted from the chain structure (see ESI for details). Here, we have used an all-electron scalar relativistic effect (SARC) basis set for Gd and DKH adapted reconstructed version of def2-type basis sets for rest of the atoms; DKH-def2-TZVP for the atoms in the first coordination sphere (N, P, and O), and DKH-def2-SVP for C, and H atoms. Scalar relativistic effects were treated by Douglas–Kroll–Hess (DKH) approximation.[51] Grimme's dispersion with Becke-Johnson damping (D3BJ) was incorporated to account for the dispersion interaction as implemented in the ORCA. [52, 53] In order to accurately estimate the sign and the magnitude of the magnetic exchange, J, the SCF iterations were executed at the "VeryTIGHTSCF" criterion without the use of auxiliary basis and convergence accelerators, as mentioned in previous studies.[54-56] The broken-symmetry DFT calculations were performed by flipping the spin on one of Gd(III) centers using the spin-flip approach as implemented in ORCA. The computed broken-symmetry calculations were verified by analyzing the spin density on individual Gd^{III} atoms. The exchange interaction $J_{Gd\text{-}Gd}$ was calculated using the Yamaguchi spin-projection formula.[57]

Results and Discussion

As mentioned above, we have observed varied coordination behavior of cyclocarbophosphazene-based ligands, which depended on the hydrolytic sensitivity of the P-N bonds involved. Thus,

while [{NP(3,5-$Me_2Pz)_2$}{NC(3,5-Me_2Pz)}$_2$] afforded a complex involving a tetrameric Cu^{II} ensemble containing P-O-P and P-O-Cu linkages[16] (Scheme S1), the reaction of [{NC(p-OC_5H_4N)}$_2${NP($NC(NMe_2)_2)_2$}] {where $NC(NMe_2)_2$ is 1,1,3,3-tetramethyl-guanidine} with $Pd(CH_3CN)_2Cl_2$ afforded a stable complex [{$NC(OC_5H_4N)$}$_2${$NP(NC(NMe_2)_2)_2$}$_3${$PdCl_2$}].[14] A few more examples of stable metal complexes with cyclocarbophosphazene derived ligand systems reported by us and others are also documented. [15, 58-61]

Furthermore, we were able to prepare hydrolytically stable multi-site coordination ligands based on the carbophosphazene platform, which was used to prepare 3d/4f heterometallic complexes.[18] With this background, we were intrigued to examine the possibility of utilizing the P-Cl containing carbophosphazene $\mathbf{L}^{PCl2}$ as the ligand. The latter was prepared by the reaction of [{NCCl}$_2${$NPCl_2$}] with $Me_2NCH_2NMe_2$. In this reaction, a selective cleavage of the C-Cl bond occurs, along with a C-N bond cleavage in the reagent, leading to an exclusive substitution at the carbon center. This reaction, developed by Elias and co-workers, is very useful in preparing carbophosphazenes with varied substituents.[62] We reasoned that $\mathbf{L}^{PCl2}$ would undergo controlled hydrolysis upon reaction with a hydrated metal salt and although the coordination behavior of such an *in situ* generated motif was not predictable *a priori* it was reasonable to assume that if both the P-Cl bonds are hydrolyzed, the resulting P(O)(OH) motif can assist the formation of a coordination polymer. This expectation was realized in the building of the 1D coordination polymers **1-4** (Scheme 2). It is to be noticed that in the coordination polymers, the carbophosphazene motif present is the hydrolyzed form of the ligand $\mathbf{L}^{PCl2}$, [{$NC(NMe_2)$}{$HNC(NMe_2)$}{P(O)(OH)}] ($\mathbf{L}^{HPO2}$). In the latter, the *in situ* generated $P(OH)_2$ undergoes a tautomerism to the observed P(O)(OH) motif. Efforts to generate the ligand $\mathbf{L}^{HPO2}$, containing the P(O)(OH) motif, directly rather than through the in situ route as described above, leads to complete degradation of the

compound. Indeed, we tried to hydrolyse the carbophosphazene ligand, $\mathbf{L}^{PCl2}$, in protic solvents such as methanol or ethanol but we observed an immediate white precipitation as soon as it is added to the corresponding alcoholic solution of lanthanide (III) nitrate hydrate salt. This may be due to the very fast hydrolysis of the P-Cl bonds. We would also like to mention that the reaction of the hydrated lanthanide salts with $\mathbf{L}^{PCl2}$ was carried out in dry methanol under inert conditions and obtained the same products as described above thus strongly implicating the water of crystallization of the lanthanide salts in the observed in situ hydrolysis of $\mathbf{L}^{PCl2}$.

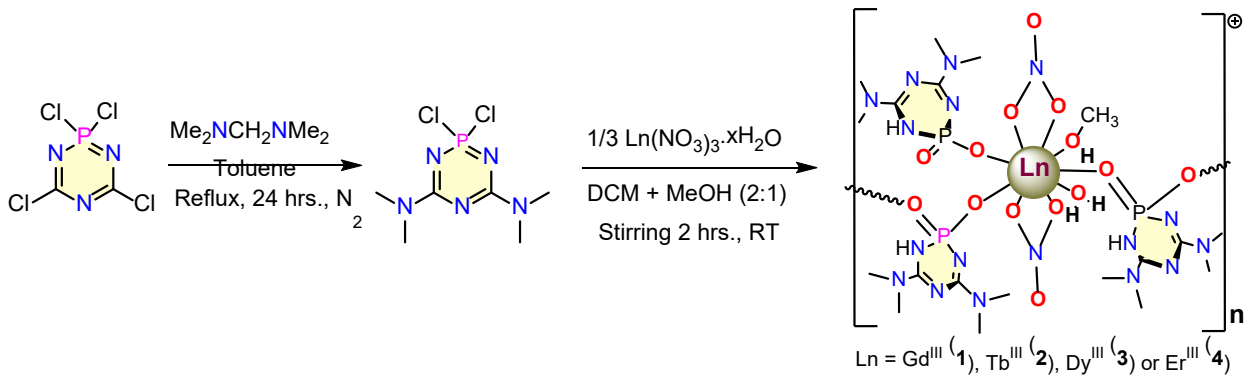

Scheme 1. General synthetic route to isolate metal complexes **1**-**4**.

X-ray crystallographic data analysis revealed that **1**-**4** are isostructural. All of them crystallized in the monoclinic, $P2_1/n$ space group. Since all four complexes (**1**-**4**) are isostructural 1D coordination polymers, **3** is chosen as a representative example to describe the structural features of these complexes. Each of the Dy^{III} centers is nine-coordinate in an *all-oxygen* coordination environment comprising of three $\mathbf{L}^{HPO2}$, one methanol, one water and two chelating nitrate ligands. The carbophosphazene $\mathbf{L}^{HPO2}$ ligands were found to provide the linkage between the Dy^{III} centres

through the repeating P-O-Dy as well as P-OH-Dy units to form a 1D coordination architecture (Figure 1). While two of the $\mathbf{L}^{HPO2}$ ligands act as bridging units between adjacent Dy^{III} centers, the third ligand uses only the P-OH unit and functions as a terminal ligand. We have witnessed the distortion and significant bond parameter changes in the rings of carbophosphazene ring after hydrolysis and coordination to Ln(III) ion in all the coordination polymers, **1**-**4**. In Scheme 3, we have compared the bond parameters of $\mathbf{L}^{PCl2}$ and its hydrolyzed form $\mathbf{L}^{HPO2}$ present in the representative structure **3**. Compared to the P-N (P1-N1 and P1-N3) bond distances of 1.577 Å in the free ligand $\mathbf{L}^{PCl2}$, these bonds are increased by ≈ 0.10 Å for $\mathbf{L}^{HPO2}$ in **3**. A slight increment in all the bond (P-N and C-N) lengths is observed in $\mathbf{L}^{HPO2}$, while from Scheme 3, it is clear that significant changes occurred in P-N bonds compared to C-N bonds. In one of the three carbophosphazene rings of the coordinated $\mathbf{L}^{HPO2}$ ligands in all the structures (ring 1), the P atom is found to highly deviate from the coplanarity with other atoms (C and N) of the ring. Due to the change in the P-N bond distances and slight distortion in the carbophosphazene ring of $\mathbf{L}^{HPO2}$, the bond angle ∠N1-P1-N3 = 97.89˚ (ring 1) and ∠N6-P2-N8 = 98.70˚ (ring 2) are found to be significantly smaller compared to $\mathbf{L}^{PCl2}$ (∠N1-P1-N3 = 117.14˚).

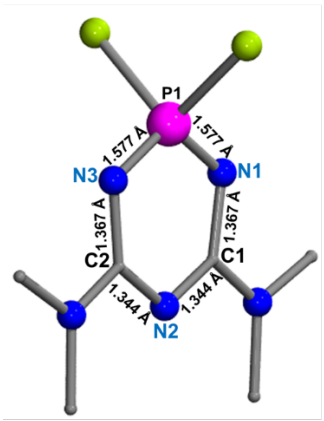

(A)

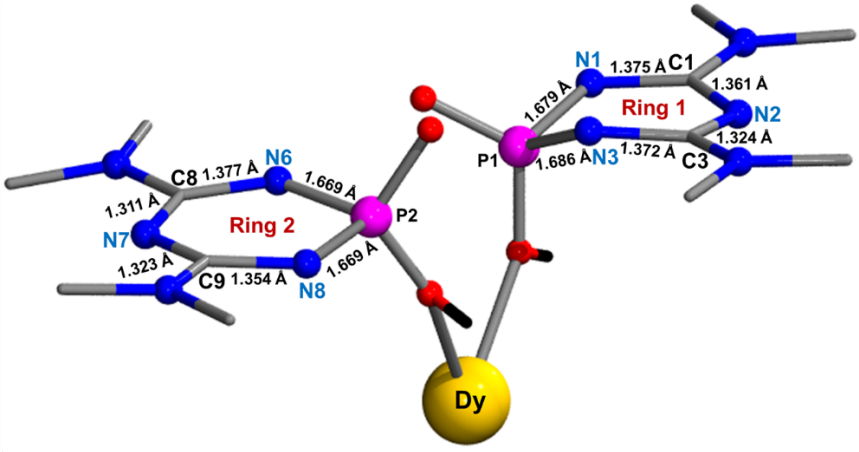

(B)

Scheme 3. The bond parameters of carbophosphazene rings in $\mathbf{L}^{PCl2}$ (A) and its hydrolyzed form $\mathbf{L}^{HPO2}$ in complex **3** (B), respectively. The other ligands around Dy^{III} ion in **3** were omitted for clarity.

These bond parameter variations are consistent with literature precedents. [14]

The P-O-Dy bond angles involved in the bridging coordination linkage are [∠P1-O(H)2-Dy1 = 138.1˚; ∠P2-O4-Dy1 = 154.8˚] and one P-O-Dy [∠P2-O5-Dy1# = 138.9˚] (where Dy1# is the symmetrically generated atom or metal center present in the extended structure). Continuous shape measurement (CShM)[63] (Table S2) confirms a small deviation from the muffin (C_s) geometry around Dy^{III}. Selected bond lengths and bond angle parameters are listed in the caption of Figure 1 while the remaining data are given in Table S3. The Dy-O bond lengths involving the $\mathbf{L}^{HPO2}$ are Dy-O2 (2.292 Å), Dy-O4 (2.358 Å) and Dy-O5 (2.420 Å). The bond lengths of Dy-O1w (2.358 Å) and Dy-O1 (2.436 Å) have been observed for Dy-O bonds involving coordinated water and methanol ligands respectively.

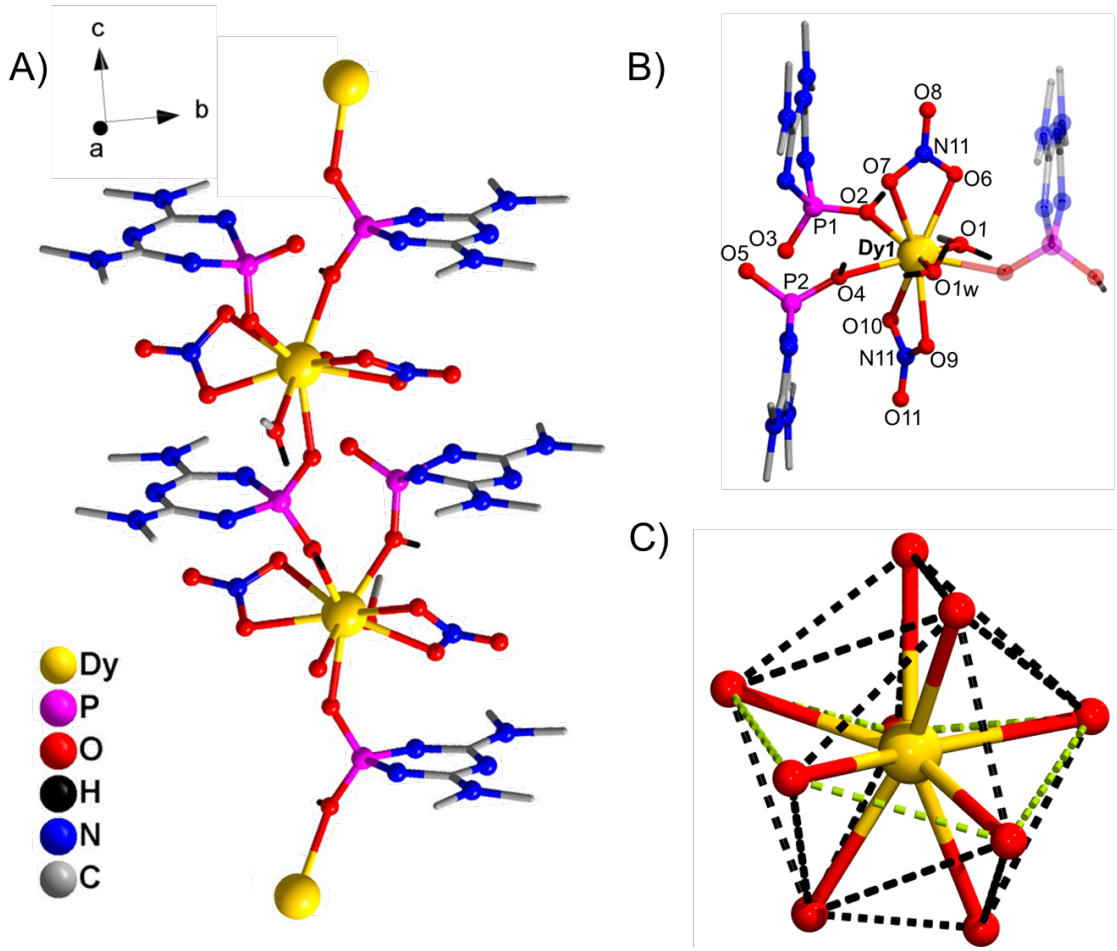

Figure 1. Ball and stick model of the crystal structure of the representative complex **3**. (A) 1D grown structure along a-axis (B) Full ligand atmosphere around Dy in which the symmetrically generated ligand is shown in transparent. Hydrogen and disordered atoms have been omitted for clarity. The muffin (Cs) geometry (C) around Dy^{III}. The connecting green broken lines in panel C is showing the distorted pentagonal arrangement of five oxygen atoms. Bond distances: Dy-O1 = 2.437 Å, Dy-O2 = 2.291 Å, Dy-O4 = 2.357Å, Dy-O5 = 2.421 Å, Dy-O6 = 2.426 Å, Dy-O7 = 2.534 Å, Dy-O9 = 2.468 Å, Dy-O10 = 2.494 Å and Dy-O1W = 2.358 Å. Bond angles: P1-O2-Dy1 = 138.09° and P2-O4-Dy1 = 154.76°

The average bond length for Dy-$O_{nitrate}$ bond is found to be 2.480 Å. A careful structural examination revealed that the five donor oxygen atoms (O1, O2, O4, O1w and O5) from ligands are found to be located at distorted pentagonal plane (D_{5h}) around Dy^{III} while four other oxygen donor atoms (O6, O7, O9 and O10) from the two chelating nitrate ligands are present above and below the pentagonal plane (Fig. 1C). This gives rise to an opportunity to replace these axial bidentate chelating nitrate ligands by monodentate, highly charge density ligands such as halides (X^-) or alkoxides ($^tBuO^-$) to generate isostructural complexes having pseudo D_{5h} geometry around Dy^{III}. This is a possibility that we plan to investigate later.

The packing diagram of **3** reveals that two single chains are found to be propagating (Fig. S2 in ESI). An intrachain hydrogen bonding is observed along the chain. The H-bonding involves the -NH part of the carbophosphazene ring with one of the oxygen donor atoms of the chelating nitrate ligand and with coordinated P=O of another carbophosphazene ligand. An average distance of 7.112 Å was observed for the intermetallic Dy···Dy separation along the polymeric chain while the closest interchain Dy···Dy distance was found to be 8.616 Å (Fig. S2 in ESI).

Magnetic Properties

Direct current (dc) magnetic susceptibility measurements were performed on the immobilized polycrystalline powder samples of **1**-**4** under an external magnetic field of 0.02 kOe, 0.2 kOe and 10 kOe in the temperature range of 2-20 K, 20-80 K and 80-300 K (Fig. 2), respectively. The observed room temperature $\chi_M T$ value of 7.81 cm^{-3} K mol^{-1} for **1** corresponds to one Gd^{III} ($^8S_{7/2}$, g_{Gd} = 2.0, $\chi_M T$ = 7.87 cm^{-3} K mol^{-1}) present in the asymmetric unit. Upon cooling, the $\chi_M T$ value was found to be almost constant down to 13 K and below this temperature the $\chi_M T$ product started decreasing and reaches a minimum value of 7.53 cm^{-3} K mol^{-1} at 2 K. The low temperature

decrease of $\chi_M T$ value can be mainly attributed to antiferromagnetic interactions. The room temperature $\chi_M T$ values of 11.51, 13.60 and 11.60 cm^{-3} K mol^{-1} respectively for **2**-**4** were found to be slightly lower (for **2** and **3**) and higher (for **4**) compared to the calculated $\chi_M T$ values of 11.82 cm^{-3} K mol^{-1} for Tb^{III} (g_{Tb} = 3/2, $^7F_6$), 14.17 for Dy^{III} (g_{Dy} = 4/3, $^6H_{15/2}$) and 11.48 cm^{-3} K mol^{-1} for Er^{III} (g_{Er} = 6/5, $^4I_{15/2}$) ion present in the respective complexes.[64] Unlike for **1** which consists of isotropic Gd^{III}, $\chi_M T$ values were found to decrease gradually down to 50 K for **2**-**4** mainly due to the depopulation of m_J levels. Upon further cooling below 50 K, fast or sudden decrease in $\chi_M T$ values were observed which reaches minimum values of 6.37, 9.16 and 6.21 cm^{-3} K mol^{-1} (for **2**-**4** respectively) at 2 K which can be attributed to the associated magnetic anisotropy and or antiferromagnetic dipolar interactions.

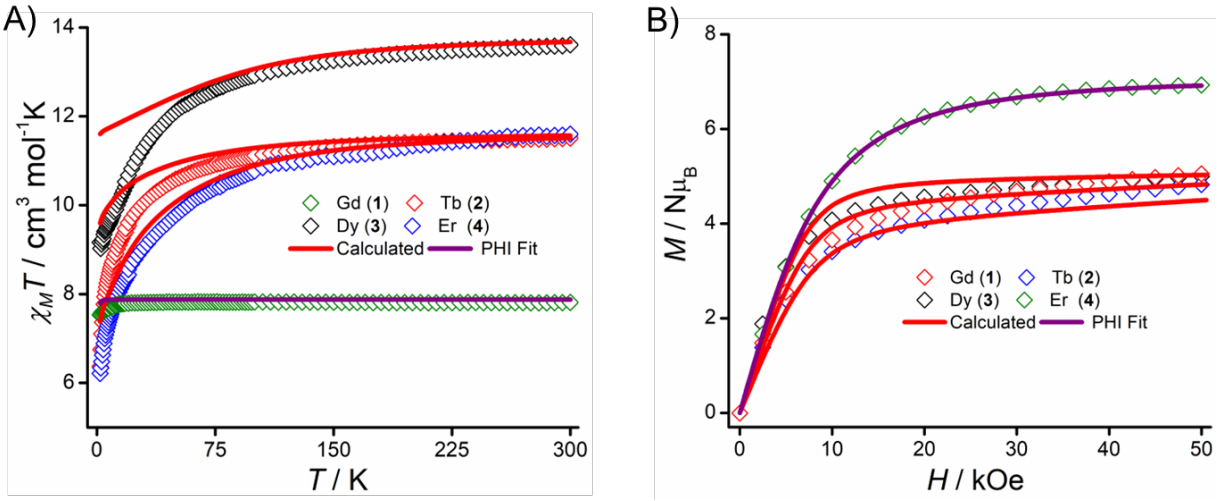

Figure 2. Direct current (dc) thermal dependence magnetic susceptibility under 1 kOe magnetic field (A) and magnetization data collected at 2 K (B) for **1**-**4**. The solid purple line represents PHI fitted data for **1** and the solid red lines represent the ab initio computed data for **2**-**4**.

The field dependent magnetization (MH = *f*(H)) measurements were performed on all the complexes **1**-**4** at 2 K (Fig. 2B). In the case of **1**, an initial linear response of magnetization was

observed with the applied magnetic field, while at the higher applied field, the magnetization gradually becomes independent of the magnetic field and reaches a saturation value of 6.91 $N\mu_B$ at 50 kOe corresponding to the ground spin state S = 7/2 (g = 2). In the case of **2**-**4** a similar response of magnetization was observed at the lower applied magnetic field as in the case of **1** and upon further increasing the magnetic field up to 50 kOe the magnetization reaches the values of 5.05, 4.99 and 4.82 $N\mu_B$ respectively without saturation. The observed lower magnetization values for **2**-**4** further suggest the presence of magnetic anisotropy in these systems due to strong spin-orbit coupling resulting from an unquenched orbital angular momentum.

To understand the SH parameters associated with Gd^{III} ion in **1**, we have fitted simultaneously magnetic susceptibility and magnetization data using PHI program.[65] The excellent fit reproduces the dc magnetic data well with g_{Gd} = 2.0 (fixed), D = 0.05 cm^{-1} and zJ = -0.002 cm^{-1} (Fig. 2). This reflects that in **1** a slight contribution of magnetic anisotropy is probably present.

In order to investigate the slow-magnetic relaxation behavior in **2**-**4** we have performed frequency dependent alternating current magnetic susceptibility measurements on their polycrystalline samples. In the absence (H_{dc} = 0 kOe) only compound **3** displayed an out-of-phase component ($\chi_M'' = f(\upsilon)$) at the highest frequencies (Fig. 3a). Under an applied external dc magnetic field ($H_{dc} \neq 0$ kOe) both compounds **3** and **4** presented χ_M'' signal sign of slow magnetic relaxation while **2** did not.

In the case of **2** no out-of-phase signals were observed both in the absence of dc field as well as on the application of dc magnetic field up to 3 kOe which corroborates that the tunnel splitting between the ground state non-KD doublets of Tb^{III} ion is very high and triggers a fast magnetic relaxation through tunneling process. The absence of field induced SMM behavior of **2** under such a high applied dc magnetic field further suggests that the energy of low-lying excited

state non KDs are not separated significantly from the ground state and allows a high tunnel splitting for magnetic relaxation.

In the case of **3**, application of the dc field led to the appearance of two distinct χ_M'' contributions at high (HF) and low frequency (LF) (Figures S3 and 3a). This indicates that a magnetic relaxation pathway through the tunneling processes (QTM) between the ground M_J states is present in **3**. The data have been analysed in the framework of the extended Debye model (Table S4) accounting for two relaxation contributions (τ) (Equation S1). The field dependence of the relaxation times is depicted in Figure 3b. A small dc field of 0.8 kOe was selected as a good compromise value. The thermal dependence of the magnetic susceptibility of **3** under an applied dc field of 0.8 kOe was measured in the frequency range of 0.1-1000 Hz (Figures S4 and 3c) and 100-10000 Hz (Figure S5). From the χ_M''(ν) plot (Figure 3c), three contributions could be identified. The data have been analysed in the framework of the extended Debye model (Table S5)[66, 67] accounting for two relaxation contributions using the Equation S1 for the 0.1-1000 Hz frequency range and in the framework of the extended Debye model (Tables S6 and S7) accounting for two single relaxation contributions using the Equation S2 for the 100-10000 Hz frequency range. The three thermal dependence of the relaxation plot (log (τ) = f(T)) at low frequency (LF), middle frequency (MF) and high frequency (HF) were fitted using the Equation 1:

$$\tau^{-1}(T,H) = AH^4T + \frac{B_1}{1+B_2H^2} + \underbrace{\tau_0^{-1}\mathrm{e}^{\left(\frac{U_{eff}}{k_BT}\right)} + CT^n}_{k(T)} \qquad \text{Eq 1.}$$

From left to right, the terms are the expressions of Direct, QTM and thermally activated (Orbach and Raman) contributions. The LF, MF and HF contributions have been fitted by considering Orbach (U_{eff} = 111(15) K, τ_o = 5.43(10) × 10^{-11}s) and Raman (C_1 = 1.33(3) × 10^{-2} s^{-1} K^{-n} and n = 6.09(21)) processes (Figure S6), Raman process (C_2 = 8.65(25) × 10^{-2} s^{-1} K^{-n} and n = 8.36(27))

only and Raman (C_3 = 13.18(11) s^{-1} K^{-n} and n = 6.81(70)) and direct (A = 1.05(1) × 10^{-8} s^{-1} K^{-1} Oe^{-m} with m = 4 (fixed)) processes (Figure S7), respectively. The n exponents are weaker than the theoretical one for a Kramer lanthanide ion (n = 9), indicating an involvement of acoustic phonons (lattice vibrations) in the Raman relaxation mechanism. Nevertheless, the n values obtained for 3 are higher than the n values found for the recent lanthanide organometallic single-molecule magnets[68-71] and one-dimensional assembly of SMM[72, 73] meaning that the role of the matrix is weak, and the Raman processes mainly involve optical phonons.

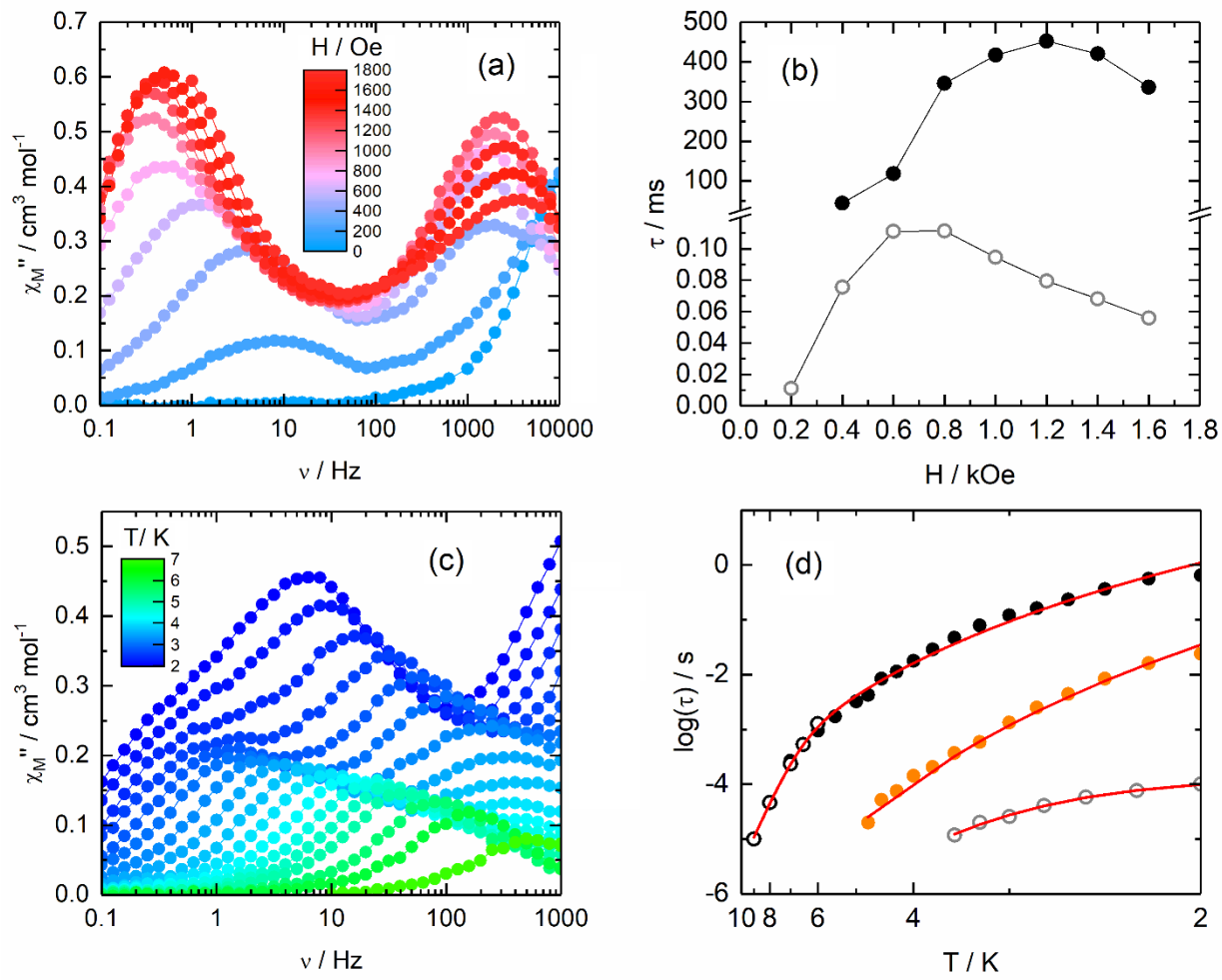

Figure 3. (a) Field dependence of the ac χ_M'' magnetic susceptibility for **3** at 2 K in the 0-1.8 kOe field range. (b) Field dependence of the relaxation times (τ) for the HF (open circles) and LF (full

black circles) contributions. (c) Frequency dependence of χ_M'' in the 2-7 K temperature range under the applied dc field of 0.8 kOe. (d) Thermal dependence of the log(τ) for the three LF (black), MF (orange), and HF (grey) contributions. Full and empty dots are data extracted from 0.1-1000 Hz squid and 100-10000 Hz PPMS measurements, respectively. Full red lines are the best-fitted curves with parameters given in the test.

In the case of **4**, slow magnetic relaxation was detected under an applied dc field (Figures S8 and 4a). Two χ_M'' contributions are growing when the applied dc field value increases. The field dependence of the relaxation time can be plotted by using the extended Debye model (Table S8), accounting for two relaxation contributions using Equation S1. The silent feature of χ_M'' signals in the absence of dc field for **4** consisting of prolate Er^{III} ion suggests the weak or insufficient charge densities provided from the equatorial ligands to favor an uniaxial magnetic anisotropy, as suggested by the computational investigation with g_x and $g_y \neq 0$, allowing an efficient magnetic relaxation through QTM. However, the application of a 2.2 kOe dc field was found to be a suitable compromise value to reduce the QTM process and induce a slow-magnetic relaxation in **4** (Figure 4b). Under such dc field, a clear frequency dependence of the magnetic susceptibility was observed (Figures S9 and 4c) with two HF and LF contributions. The data have been analyzed in the framework of the extended Debye model (Table S8), accounting for two relaxation contributions using Equation S1. The best fit of the log(τ) vs T plot for the LF contribution was obtained with a combination of Orbach (U_{eff} = 40.8(8) K and $\tau_o = 5.73(14) \times 10^{-10}$ s) and direct ($A = 6.45(3) \times 10^{-12}$ s^{-1} K^{-1} Oe^{-m} with m = 4 (fixed)) relaxation processes (Figure 4d).

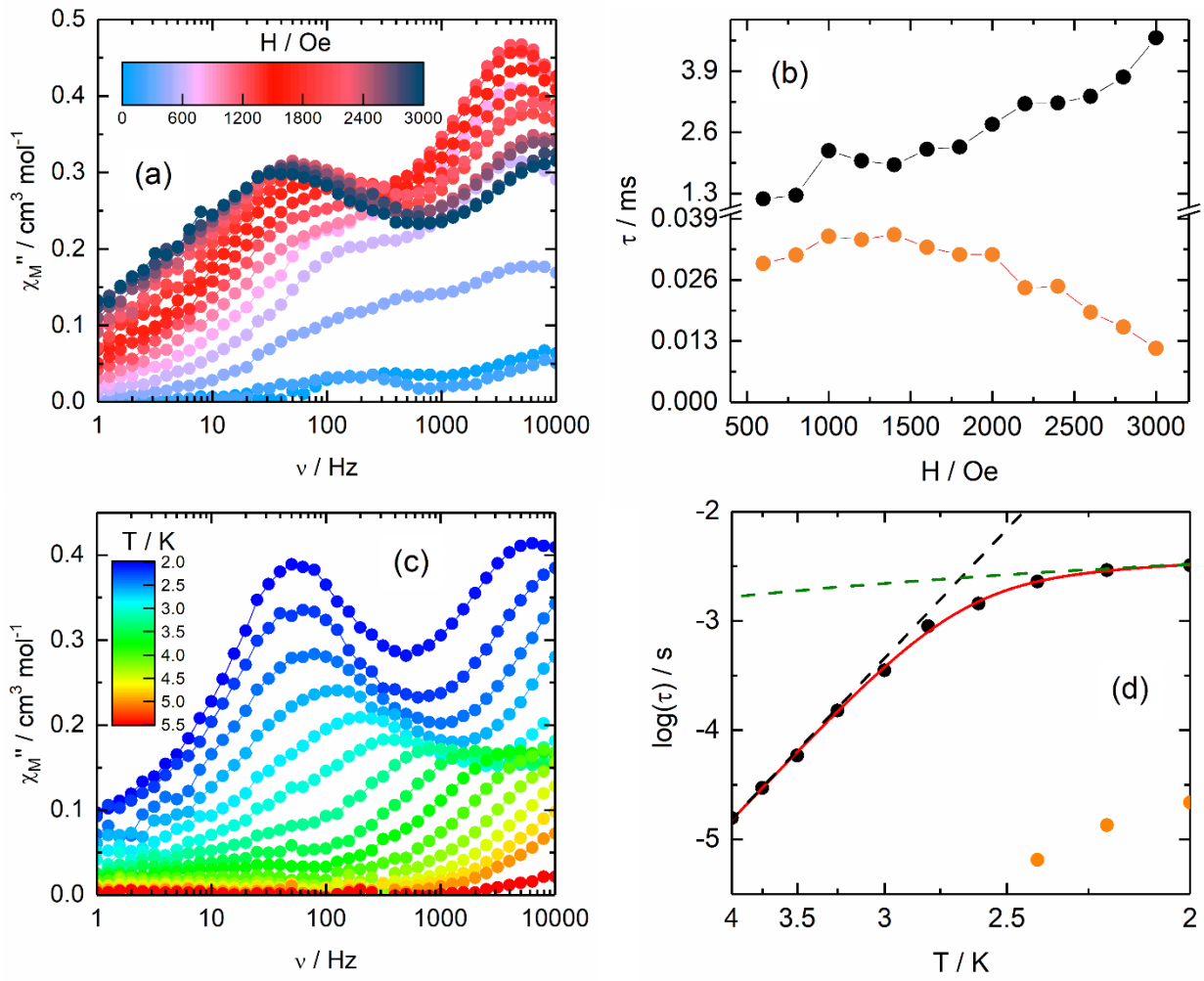

Figure 4. (a) Field dependence of the ac χ_M'' magnetic susceptibility for **4** at 2 K in the 0-3 kOe field range. (b) Field dependence of the relaxation times (τ) for the HF (orange circles) and LF (full black circles) contributions. (c) Frequency dependence of χ_M'' in the 2-5.5 K temperature range under the applied dc field of 2.2 kOe. (d) Thermal dependence of the log(τ) for the two LF (black dots) and HF (orange dots) contributions. The whole red line is the best-fitted curve with the parameters given in the test. Orbach and Direct contribution are represented in dashed black and green lines, respectively.

The presence of multiple out-of-phase magnetic susceptibility contributions could be attributed to Ln(III) ions in different coordination environments[74, 75] crystallographically independent Ln^{III} ions[76], or to the presence of significant dipolar interaction.[77] The latter origin could be discarded because the ac magnetic susceptibility was carried out under an applied dc field. Nevertheless taking into account that the ac magnetic susceptibility was measured at low temperature while the X-ray structure was refine at room temperature, the presence of several lanthanide centres with different geometries at low temperature might not be rule out because lowering temperature could lead to significant change of the geometry of lanthanide ions.[78] Moreover the presence of multiple χ_M" contributions might be attributed to an intramolecular mechanism of multiple relaxation times at the single ion level because several relaxation modes might exist in the systems, as demonstrated by L. F. Chibotaru and Coll.[79] To the best of our knowledge, that is the first time that three distinct relaxation times are identified in the experimental frequency range for a Dy(III) compound. Nevertheless, the origin of such multiple χ_M" contributions cannot be unambiguously determined at this stage.

Computational Studies on 1-4

To shed light on the origin of magnetic anisotropy of Ln(III) ions and rationalize the slow magnetic relaxation observed in **2**-**4**, we carried out CASSCF-based *ab initio* calculations on the X-ray crystal structures (see computational methodology for details). Here, we have used mononuclear model complexes of coordination polymers **2**-**4** (see Figure S10 in the ESI for model structure), computed the SH parameters of individual ions, and analyzed the nature of magnetic anisotropy and how it is associated with slow relaxation. In complex **2**, the Tb(III) is a non-Kramers ion possessing a $4f^8$ electronic configuration with a ^7F ground state configuration. For Tb^{III}, CASSCF

computed spin-free septet spans over a range of ~ 565 $cm^{-1,}$ while the computed 140 quintets range from ~25660 cm^{-1} to ~95574 cm^{-1} (see Table S10). The first excited spin-free septet state is placed at ~ 91 cm^{-1} above the ground state. SO-RASSI computed spin-orbit spectrum corresponding to the $^7F_6$ ground state spans over a range of ~ 300.5 cm^{-1}. The computed g-value (g_{zz}) for the ground state pseudo-Kramers doublet (pseudo-KD) is ~17.625, representing an Ising-type anisotropy. The computed g-tensor and energies of the low-lying pseudo-KDs are provided in Table S13. A wavefunction decomposition analysis indicates the ground state to be primarily m_J |±6⟩: 95.9%|±6⟩ + 3.4% |±4⟩ with a small admixing from the other 3.4% |±4⟩ excited pseudo-KD. This small admixing results in a non-negligible tunnel splitting of 0.28 cm^{-1}, which is significant enough to induce the quantum tunneling of magnetization (QTM) within the ground state pseudo-KD. The orientation of the ground state g_{zz} axis nearly passes through one of the farthest -O atoms (~ 30 degrees) of the attached nitrate ligand. The first excited pseudo-KD is primarily m_J |±5⟩: 33.4%|±5⟩ + 27.3% |±4⟩ +23.5% |±3⟩ + 10.2% |±2⟩ (see Table S17), which is heavily mixed with other low-lying excited pseudo-KDs resulting in a significant tunnel splitting of the ~0.9 cm^{-1} for the first excited pseudo-KD. The non-collinearity in the main anisotropic axes (g_{zz}) of the ground and first excited pseudo-KD, along with significantly large tunnel splitting for the first excited KD, indicates that the magnetic relaxation will likely occur through the first excited pseudo-KD. This suggests a theoretical barrier height of ~35 cm^{-1} for **2**. Moreover, the reasonably large tunnel splitting value within the ground state (0.28 cm^{-1}) indicates the presence of the QTM. The smaller gap between the ground and first excited pseudo-KD and associated large tunnel splitting suggests that the ligand field lacks a higher axial environment. The large extent of QTM and a small barrier for TA-QTM via the first excited pseudo-KD indicates why complex **2** lacks any SMM characteristics.

On the other hand, Dy^{III} and Er^{III} are the natural targets for designing SMMs with high blocking temperatures by virtue of being Kramers ions. However, the ligand field criteria for achieving the large barrier height for Dy^{III} and Er^{III} are opposite to each other due to the differences in the electron cloud shape of these ions (oblate/prolate).[80, 81] For oblate type Dy^{III} ion in complex **3**, the CASSCF computed spin-free sextet states span over an energy window of ~ 35348 cm^{-1}, with the first excited KD ~ 9 cm^{-1} higher in energy from the ground state. SO-RASSI computed energy of the low-lying eight KDs generated from the $^6H_{15/2}$ ground state spans over a range of ~ 486 $cm^{-1,}$ with the first excited KD at ~ 152 cm^{-1} (Table S11). CASSCF computed low-lying SOC energy spectrum, and associated g-tensors for Dy^{III} ion in **3** are listed in Table S14. The computed ground state g-values are highly axial in nature (g_{xx} = 0.0298, g_{yy} = 0.0440 and g_{zz} = 19.5632) and indicate the stabilization of the m_J $|\pm15/2\rangle$ with a small admixture (3.0%) of the $|\pm9/2\rangle$ excited state (see Table S18). On the other hand, for **4**, the energies for the low-lying eight KDs emerging from the $^4I_{15/2}$ ground state span over an energy range of ~ 329 cm^{-1}, with the first excited KD being located at ~ 42 cm^{-1} higher in energy from the ground state (Table S12). Our calculations revealed axiality in the ground state g-values (g_{xx} = 0.965, g_{yy}= 1.931 and g_{zz} = 15.056), with a dominant transverse component in the g-value (g_{xx} and g_{yy} >> 0) for complex **4** (Table S15). Decomposition of the ground state wavefunction indicates stabilization of m_J $|\pm15/2\rangle$: **67.8% $|\pm15/2\rangle$**+ 11.3% $|\pm9/2\rangle$ + 7.5% $|\pm11/2\rangle$, primarily as the ground state, which is largely mixed with other excited states (see Table S19). For complex **3**, the main anisotropic axis (g_{zz}) is oriented towards the attached -NO_3 ligand perpendicular to the equatorial plane formed for three carbophosphazene ligands, water, and methanol molecules coordinated to the Dy(III) ion. The CASSCF computed beta spin density shows a typical disk-type feature located mainly on this equatorial plane (see Figure 5). Alongside, the CASSCF computed Loprop charges on the axial atoms (-O from NO_3 ligands) are smaller than

the Loprop charges present on the other ligands, which further supports the preference of the g-tensor orientation along the minimum electrostatic region in **3** (see Figure S12 in ESI). Contrarily for **4**, we have noticed that the ground state g-tensor is oriented towards the weakly coordinated -H_2O molecule and is in line with prolate type electron cloud shape. The computed beta-spin density for **4** lacks a prolate-type electron cloud shape; it rather shows a spherical shape, indicating an unfavorable ligand field for maximizing the magnetic anisotropy of Er(III) ions. Due to non-collinearity in the computed main magnetic axes (g_{zz}) of the ground and first excited KD, the magnetic relaxation is likely to occur via the first excited KD for models **3** and **4**. This sets the theoretical barrier height (U_{cal}) to be ~ 152 cm^{-1} and ~ 42 cm^{-1} for **3** and **4,** respectively. Additionally, the presence of a transverse component in the ground state g-values for both **3**-**4** indicates the quantum tunneling of magnetization (QTM) as another prominent pathway for magnetic relaxation. The significantly large transverse g-values for **4** suggest that the extent of QTM is expected to be significantly large in this complex compared to **3**. Alongside, the computed experimental static *dc* magnetic properties (magnetic susceptibility and magnetization data) are in reasonably good agreement with the experimental data, highlighting the goodness of the computed spin-Hamiltonian (SH) parameters. Moreover, the lower experimental energy barrier values for **3** (77.1 cm^{-1}) and **4** (28.4 cm^{-1}) compared to the computational ones can be reasonably explained by the involvement of under-energy barrier magnetic relaxation processes such as Raman and direct.

Due to the muffin-like *Cs* geometry around Ln^{III} ions, it is very difficult to predict the suitability of the ligand field of the oblate/prolate type ions. Thus, to gain insight into the nature of the ligand field and its suitability with Ln^{III} ions, we have analyzed the crystal field parameters (CF) as implemented in MOLCAS. In the SINGLE_ANISO module, the CF parameters are computed using the following Hamiltonian,

$$\widehat{H_{CF}} = \sum\sum_{k=-q}^{q} B_k^q \, O_k^q \ldots\ldots(1)$$

where B_k^q and O_k^q are the crystal field parameters and Stevens' operator, respectively. The computed CF parameters have been widely used to predict the nature of the ligand field (axial vs. nonaxial) and how it affects the associated QTM in various mononuclear lanthanide-based single-molecule magnets.[40, 81-86] The axial component of the CF parameters, i.e., B_k^q (where k = 2, 4 6 and q = 0) is used as a marker to predict the axial behavior of the ground state m_J level of the metal ion concerning the ligand field. Our computed CF parameters for **2**-**4** indicate that both the axial and nonaxial terms (where q $\neq$ 0) B_k^q parameters are of comparable strengths in all the cases. This indicates that the ligand field offered is not suitable for stabilizing the pure largest m_J state of Tb^{III}, Dy^{III}, and Er^{III} ions. This is in accordance with the muffin type (Cs) geometry (low-symmetry) that lacks any suitable ligand field to stabilize either prolate/oblate ion specifically. Moreover, among **2**-**4**, the values of the axial term B_2^0 are -2.4, -3.70 and -0.65 for Tb^{III}, Dy^{III}, and Er^{III} ions respectively (see Table S16). The computed B_2^0 value for oblate type Tb^{III} and Dy^{III} ion is much larger compared to prolate type Er^{III} ion, indicating a comparatively stronger axial ligand field for oblate type ions. Alongside, the largest value of B_2^0 for Dy^{III} among **2**-**4** indicates that the ligand field preferably offers more axiality for Dy^{III}, suppressing the QTM to a large extent in **3** compared to **2** and **4**. The observed trends in CF parameters corroborate why zero-field out-of-phase magnetic susceptibility signals are absent in **2** and **4**.

To shed light on the nature of magnetic relaxation, we have also computed the ab initio blockade barrier for all three complexes. The calculated transverse magnetic moment between the ground state KDs is very large ~1.2E-02μ_B (0.48 μ_B) (usually <10E-06 for complete quenching of QTM) for Dy^{III} and (Er^{III}), respectively in **3** and **4**.[87-93] This indicates that QTM is one of the plausible

mechanisms for magnetic relaxation in **3** and **4**; however, it is the most dominating mechanism for **4**. For **2**, we have noticed a large tunnel splitting the value of ~ 0.3 $cm^{-1,}$ indicative of a large QTM (~10E-3 for top-performing Tb-based SIMs) [94-96] within the ground state. On the other hand, the computed transverse magnetic moment between the ground and first excited KDs is significantly larger than the number connecting ground state doublet for all the complexes. This indicates that the major relaxation pathway in all the complexes occurs via the first excited KD (see Figure 5). The matrix element joining the first excited KD (green color in Figure 5) represents the TA-QTM pathway via this KD. The non-collinearity between the ground and excited KDs sets the theoretical barrier height of ~152 cm^{-1} (42 cm^{-1}) for complexes **3** (**4**), respectively. For **2**, the theoretical barrier height was observed to be ~ 35 cm^{-1} and with a tunnel splitting of 0.9 cm^{-1}, indicative of dominant relaxation via the first excited pseudo-KD. The computed magnetic relaxation pattern agrees well with the experimental observation where **3** shows zero-field relaxation, while the giant QTM (tunnel splitting) within the ground state diminishes zero SMM behavior for **3** and **4**.

The further proceeding attempt was to determine the isotropic magnetic exchange interaction between the Gd^{III} centers in **1** using the ORCA 4.2.1 software suite. These calculations were carried out using broken-symmetry density functional theory (BS-DFT) analysis on the dimeric model complex extracted from the chain structure (see Figure S10), as detailed in the section on computational methodology. These broken-symmetry DFT calculations have shown a track record in computing the sign and magnitude of the magnetic exchange interaction in various binuclear/polynuclear lanthanide-based complexes.[42, 43, 97-100] The results obtained from the BS-DFT calculations indicate a weak antiferromagnetic interaction strength of -0.00049cm^{-1} between the intrachain Gd^{III} centers. This weak interaction can be due to the significant separation (~7.172 Å) between the two Gd^{III} centers, which are bridged by the P(O)(OH) motif. The overlap integrals

between the corresponding 4f-orbitals were computed, and no such substantial overlaps were found among the seven corresponding 4f-orbitals (see Figure S13 and Table S20), which is in line with observed antiferromagnetic interaction. Analysis of the spin density depicts that the Gd(III) centers have a spin density of ~7.02, the result of quite a modest spin polarization (Figure S14).

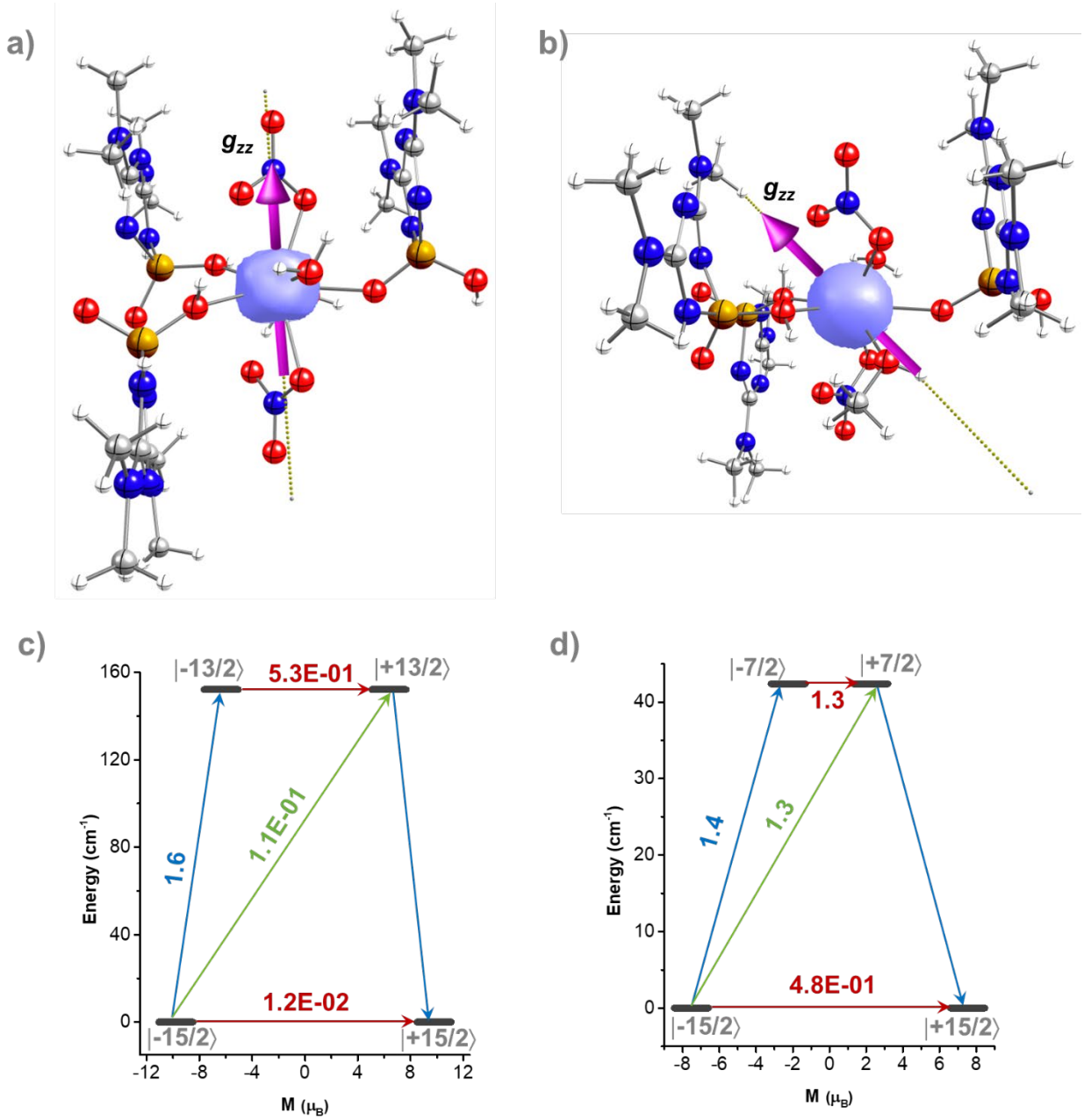

Figure 5. CASSCF computed the orientation of the main magnetic axes (g_{zz}) along with beta-spin density for a) complex **3** and b) complex **4**. CASCCF computed blockade barrier c) for **3** and d) for **4**. The dark grey horizontal bars indicate the KDs as magnetic moments' function. The red, blue, and green arrows represent the possible QTM/TA-QTM, Orbach, and Raman relaxation pathways. The corresponding-colored numbers are transverse magnetic moments representing the possibilities for the pathway.

Conclusion

We have isolated a series of novel 1D chains of Ln^{III} {where Ln^{III} = Gd (**1**), Tb(**2**), Dy(**3**), Er(**4**)} coordination polymers through an *in situ* hydrolysis of P-Cl bonds of carbophosphazene ligand. Dynamic magnetic studies revealed that Dy^{III} and Er^{III} analogs show field-induced slow magnetic relaxation behavior under an applied dc magnetic field of 0.8 kOe and 2.2 kOe, respectively. An unprecedented triple magnetic relaxation contribution was observed in the case of $Dy^{III,}$ while two for Er^{III} analogs, respectively. We have rationalized our experimental findings with BS-DFT and CASSCF/SO-RASSI/SINGLE_ANISO theoretical calculations.

Acknowledgements

VC thanks the Department of Science and Technology (DST), India for J. C. Bose fellowship. FP thanks the CNRS, Université de Rennes 1, and the European Commission through the ERC-CoG 725184 MULTIPROSMM (project no. 725184) for financial support. NA thanks Tata Institute of Fundamental Research Hyderabad for Postdoctoral Research Fellowships. SKS and PPS acknowledge the Department of Science and Technology for the Start-up Research Grant (SRG/2020/001323) and IIT Hyderabad for generous funding. The support and resources provided by PARAM SEVA Facility under the National Supercomputing Mission, Government of India at

the Indian Institute of Technology, Hyderabad, are gratefully acknowledged. SKS also acknowledges Prof. Gopalan Rajaraman, IIT Bombay, for providing the MOLCAS 8.2 code facility. Finally, SKS and PPS also acknowledge Prof. Federico Totti, University of Florence for valuable discussion.

References:

1. C. W. Allen, Regio-and stereochemical control in substitution reactions of cyclophosphazenes, *Chem. Rev.*, 1991, **91**, 119-135.
2. M. Witt and H. W. Roesky, Transition and main group metals in cyclic phosphazanes and phosphazenes, *Chem. Rev.*, 1994, **94**, 1163-1181.
3. A. Steiner, S. Zacchini and P. I. Richards, From neutral iminophosphoranes to multianionic phosphazenates. The coordination chemistry of imino–aza-P(V) ligands, *Coord. Chem. Rev.*, 2002, **227**, 193-216.
4. A. J. Elias and J. n. M. Shreeve, in *Adv. Inorg. Chem.*, Academic Press, 2001, vol. 52, pp. 335-358.
5. V. Chandrasekhar and B. Murugesapandian, Phosphorus-Supported Ligands for the Assembly of Multimetal Architectures, *Acc. Chem. Res.*, 2009, **42**, 1047-1062.
6. V. Chandrasekhar, P. Thilagar and B. Murugesa Pandian, Cyclophosphazene-based multi-site coordination ligands, *Coord. Chem. Rev.*, 2007, **251**, 1045-1074.
7. V. Chandrasekhar and S. Nagendran, Phosphazenes as scaffolds for the construction of multi-site coordination ligands, *Chem. Soc. Rev.*, 2001, **30**, 193-203.
8. A. Chakraborty, N. Ahmed and V. Chandrasekhar, in *Organophosphorus Chemistry: Volume 50*, The Royal Society of Chemistry, 2021, vol. 50, pp. 429-466.
9. V. Chandrasekhar and A. Chakraborty, in *Organophosphorus Chemistry: Volume 48*, The Royal Society of Chemistry, 2019, vol. 48, pp. 400-423.
10. I. Manners, Sulfur-nitrogen-phosphorus polymers, *Coord. Chem. Rev.*, 1994, **137**, 109-129.
11. S. Rothemund and I. Teasdale, Preparation of polyphosphazenes: a tutorial review, *Chem. Soc. Rev.*, 2016, **45**, 5200-5215.
12. H. R. Allcock, S. M. Coley, I. Manners, K. B. Visscher, M. Parvez, O. Nuyken and G. Renner, Reactivity and polymerization behavior of a pentachlorocyclocarbophosphazene, N3P2CCl5, *Inorg. Chem.*, 1993, **32**, 5088-5094.
13. N. Dastagiri Reddy, A. J. Elias and A. Vij, Novel ferrocene derived cyclocarbaphosphazenes: synthesis and structure of spiro {Fe(η-C_5H_5)-[η-$C_5H_4CH_2P(S)(CH_2O)_2PN$]}$(Me_2NCN)_2$, *Inorg. Chem. Commun.*, 2000, **3**, 29-31.
14. V. Chandrasekhar, V. Krishnan, R. Azhakar, T. Senapati, A. Dey and R. Suriya Narayanan, Carbophosphazene-Supported Ligand Systems Containing Pyrazole/Guanidine Coordinating Groups, *Inorg. Chem.*, 2011, **50**, 2568-2579.
15. T. Senapati, A. Dey, V. Kumar and V. Chandrasekhar, Metalation Studies of Carbophosphazene-Based Coordination Ligands: Metallacages to Polymeric Networks, *Cryst. Growth Des.*, 2020, **20**, 2660-2669.
16. V. Chandrasekhar, R. Azhakar, V. Krishnan, A. Athimoolam and B. M. Pandian, Cyclocarbophosphazene-Containing Tetrameric Assemblies Formed by the Mediation of P−O−P and P−O−Cu Linkages, *J. Am. Chem. Soc.*, 2006, **128**, 6802-6803.

17. V. Chandrasekhar, T. Senapati, A. Dey, S. Das, M. Kalisz and R. Clérac, Cyclo- and Carbophosphazene-Supported Ligands for the Assembly of Heterometallic (Cu2+/Ca2+, Cu2+/Dy3+, Cu2+/Tb3+) Complexes: Synthesis, Structure, and Magnetism, *Inorg. Chem.*, 2012, **51**, 2031-2038.
18. A. Chakraborty, N. Ahmed, J. Ali, S. Moorthy, J. Goura, S. K. Singh, G. Rogez and V. Chandrasekhar, Exchange-driven slow relaxation of magnetization in $Ni^{II}_2Ln^{III}_2$ (Ln^{III} = Y, Gd, Tb and Dy) butterfly complexes: experimental and theoretical studies, *Dalton Trans.*, 2022, **51**, 14721-14733.
19. P. Kumar, S. Biswas, A. Swain, J. Acharya, V. Kumar, P. Kalita, J. F. Gonzalez, O. Cador, F. Pointillart, G. Rajaraman and V. Chandrasekhar, Azide-Coordination in Homometallic Dinuclear Lanthanide(III) Complexes Containing Nonequivalent Lanthanide Metal Ions: Zero-Field SMM Behavior in the Dysprosium Analogue, *Inorg. Chem.*, 2021, **60**, 8530-8545.
20. S. Das, A. Dey, S. Biswas, E. Colacio and V. Chandrasekhar, Hydroxide-Free Cubane-Shaped Tetranuclear [Ln4] Complexes, *Inorg. Chem.*, 2014, **53**, 3417-3426.
21. P. Kalita, N. Ahmed, S. Moorthy, V. Béreau, A. K. Bar, P. Kumar, P. Nayak, J.-P. Sutter, S. K. Singh and V. Chandrasekhar, Slow magnetic relaxation in a homoaxially phosphine oxide coordinated pentagonal bipyramidal Dy(iii) complex, *Dalton Trans.*, 2023, **52**, 2804-2815.
22. A. K. Bar, P. Kalita, J.-P. Sutter and V. Chandrasekhar, Pentagonal-Bipyramid Ln(III) Complexes Exhibiting Single-Ion-Magnet Behavior: A Rational Synthetic Approach for a Rigid Equatorial Plane, *Inorg. Chem.*, 2018, **57**, 2398-2401.
23. P. Kalita, N. Ahmed, A. K. Bar, S. Dey, A. Jana, G. Rajaraman, J.-P. Sutter and V. Chandrasekhar, Pentagonal Bipyramidal Ln(III) Complexes Containing an Axial Phosphine Oxide Ligand: Field-induced Single-ion Magnetism Behavior of the Dy(III) Analogues, *Inorg. Chem.*, 2020, **59**, 6603-6612.
24. O. V. Dolomanov, L. J. Bourhis, R. J. Gildea, J. A. Howard and H. Puschmann, OLEX2: a complete structure solution, refinement and analysis program, *J. Appl. Crystallogr.*, 2009, **42**, 339-341.
25. G. M. Sheldrick, SHELXT–Integrated space-group and crystal-structure determination, *Acta Crystallogr., Sect. A: Found. Adv.*, 2015, **71**, 3-8.
26. G. M. Sheldrick, Crystal structure refinement with SHELXL, *Acta Crystallogr., Sect. C: Struct. Chem.*, 2015, **71**, 3-8.
27. B. O. Roos, P. R. Taylor and P. E. M. Sigbahn, A complete active space SCF method (CASSCF) using a density matrix formulated super-CI approach, *Chem. Phys.*, 1980, **48**, 157-173.
28. F. Aquilante, J. Autschbach, R. K. Carlson, L. F. Chibotaru, M. G. Delcey, L. De Vico, I. Fdez. Galván, N. Ferré, L. M. Frutos, L. Gagliardi, M. Garavelli, A. Giussani, C. E. Hoyer, G. Li Manni, H. Lischka, D. Ma, P. Å. Malmqvist, T. Müller, A. Nenov, M. Olivucci, T. B. Pedersen, D. Peng, F. Plasser, B. Pritchard, M. Reiher, I. Rivalta, I. Schapiro, J. Segarra-Martí, M. Stenrup, D. G. Truhlar, L. Ungur, A. Valentini, S. Vancoillie, V. Veryazov, V. P. Vysotskiy, O. Weingart, F. Zapata and R. Lindh, Molcas 8: New capabilities for multiconfigurational quantum chemical calculations across the periodic table, *J. Comput. Chem.*, 2016, **37**, 506-541.
29. A. D. Becke, Density-functional exchange-energy approximation with correct asymptotic behavior, *Phys. Rev. A*, 1988, **38**, 3098-3100.
30. J. P. Perdew, Density-functional approximation for the correlation energy of the inhomogeneous electron gas, *Phys. Rev. B*, 1986, **33**, 8822-8824.
31. F. Weigend, Accurate Coulomb-fitting basis sets for H to Rn, *Phys. Chem. Chem. Phys.*, 2006, **8**, 1057-1065.
32. F. Weigend and R. Ahlrichs, Balanced basis sets of split valence, triple zeta valence and quadruple zeta valence quality for H to Rn: Design and assessment of accuracy, *Phys. Chem. Chem. Phys.*, 2005, **7**, 3297-3305.

33. B. O. Roos, V. Veryazov and P.-O. Widmark, Relativistic atomic natural orbital type basis sets for the alkaline and alkaline-earth atoms applied to the ground-state potentials for the corresponding dimers, *Theor. Chem. Acc.*, 2004, **111**, 345-351.
34. B. O. Roos, R. Lindh, P.-Å. Malmqvist, V. Veryazov, P.-O. Widmark and A. C. Borin, New Relativistic Atomic Natural Orbital Basis Sets for Lanthanide Atoms with Applications to the Ce Diatom and LuF3, *J. Phys. Chem. A*, 2008, **112**, 11431-11435.
35. G. Cucinotta, M. Perfetti, J. Luzon, M. Etienne, P. E. Car, A. Caneschi, G. Calvez, K. Bernot and R. Sessoli, Magnetic anisotropy in a dysprosium/DOTA single-molecule magnet: beyond simple magneto-structural correlations, *Angew. Chem., Int. Ed.*, 2012, **51**, 1606-1610.
36. K. Bernot, J. Luzon, L. Bogani, M. Etienne, C. Sangregorio, M. Shanmugam, A. Caneschi, R. Sessoli and D. Gatteschi, Magnetic anisotropy of dysprosium (III) in a low-symmetry environment: a theoretical and experimental investigation, *J. Am. Chem. Soc.*, 2009, **131**, 5573-5579.
37. M. Briganti, G. F. Garcia, J. Jung, R. Sessoli, B. Le Guennic and F. Totti, Covalency and magnetic anisotropy in lanthanide single molecule magnets: the DyDOTA archetype, *Chem. Sci.*, 2019, **10**, 7233-7245.
38. M. Briganti, E. Lucaccini, L. Chelazzi, S. Ciattini, L. Sorace, R. Sessoli, F. Totti and M. Perfetti, Magnetic anisotropy trends along a full 4f-series: the f^{n+7} effect, *J. Am. Chem. Soc.*, 2021, **143**, 8108-8115.
39. F. S. Santana, M. Perfetti, M. Briganti, F. Sacco, G. Poneti, E. Ravera, J. F. Soares and R. Sessoli, A dysprosium single molecule magnet outperforming current pseudocontact shift agents, *Chem. Sci.*, 2022, **13**, 5860-5871.
40. S. K. Singh, T. Gupta, M. Shanmugam and G. Rajaraman, Unprecedented magnetic relaxation via the fourth excited state in low-coordinate lanthanide single-ion magnets: a theoretical perspective, *Chem. Commun.*, 2014, **50**, 15513-15516.
41. J. Acharya, N. Ahmed, J. F. Gonzalez, P. Kumar, O. Cador, S. K. Singh, F. Pointillart and V. Chandrasekhar, Slow magnetic relaxation in a homo dinuclear Dy (III) complex in a pentagonal bipyramidal geometry, *Dalton Trans.*, 2020, **49**, 13110-13122.
42. S. Roy, P. Shukla, P. Prakash Sahu, Y. C. Sun, N. Ahmed, S. Chandra Sahoo, X. Y. Wang, S. Kumar Singh and S. Das, Zero-field Slow Magnetic Relaxation Behavior of Dy_2 in a Series of Dinuclear $\{Ln_2\}$(Ln= Dy, Tb, Gd and Er) Complexes: A Combined Experimental and Theoretical Study, *Eur. J. Inorg. Chem.*, 2022, **2022**, e202100983.
43. P. Kumar, J. F. Gonzalez, P. P. Sahu, N. Ahmed, J. Acharya, V. Kumar, O. Cador, F. Pointillart, S. K. Singh and V. Chandrasekhar, Magnetocaloric effect and slow magnetic relaxation in peroxide-assisted tetranuclear lanthanide assemblies, *Inorg. Chem. Front.*, 2022, **9**, 5072-5092.
44. D. Shao, P. P. Sahu, W.-J. Tang, Y.-L. Zhang, Y. Zhou, F.-X. Xu, X.-Q. Wei, Z. Tian, S. K. Singh and X.-Y. Wang, A single-ion magnet building block strategy toward Dy 2 single-molecule magnets with enhanced magnetic performance, *Dalton Trans.*, 2022, **51**, 18610-18621.
45. P. Å. Malmqvist, B. O. Roos and B. Schimmelpfennig, The restricted active space (RAS) state interaction approach with spin–orbit coupling, *Chem. Phys. Lett.*, 2002, **357**, 230-240.
46. L. F. Chibotaru and L. Ungur, Ab initio calculation of anisotropic magnetic properties of complexes. I. Unique definition of pseudospin Hamiltonians and their derivation, *J. Chem. Phys.*, 2012, **137**.
47. F. Aquilante, R. Lindh and T. Bondo Pedersen, Unbiased auxiliary basis sets for accurate two-electron integral approximations, *J. Chem. Phys.*, 2007, **127**, 114107.
48. F. Neese, Software update: the ORCA program system, version 4.0, *Wiley Interdiscip. Rev.: Comput. Mol. Sci.*, 2018, **8**, e1327.
49. F. Neese, F. Wennmohs, U. Becker and C. Riplinger, The ORCA quantum chemistry program package, *J. Chem. Phys.*, 2020, **152**, 224108.

50. A. D. Becke, Density-functional thermochemistry. III. The role of exact exchange, *J. Chem. Phys.*, 1993, **98**, 5648-5652.
51. B. A. Hess, Relativistic electronic-structure calculations employing a two-component no-pair formalism with external-field projection operators, *Phys. Rev. A*, 1986, **33**, 3742.
52. S. Grimme, J. Antony, S. Ehrlich and H. Krieg, A consistent and accurate ab initio parametrization of density functional dispersion correction (DFT-D) for the 94 elements H-Pu, *J. Chem. Phys.*, 2010, **132**, 154104.
53. S. Grimme, S. Ehrlich and L. Goerigk, Effect of the damping function in dispersion corrected density functional theory, *J. Comput. Chem.*, 2011, **32**, 1456-1465.
54. D. Ranieri, F. Santanni, A. Privitera, A. Albino, E. Salvadori, M. Chiesa, F. Totti, L. Sorace and R. Sessoli, An exchange coupled meso–meso linked vanadyl porphyrin dimer for quantum information processing, *Chem. Sci.*, 2023, **14**, 61-69.
55. A. Bencini and F. Totti, A Few Comments on the Application of Density Functional Theory to the Calculation of the Magnetic Structure of Oligo-Nuclear Transition Metal Clusters, *J. Chem. Theory Comput.*, 2009, **5**, 144-154.
56. D. Ranieri, A. Privitera, F. Santanni, K. Urbanska, G. J. Strachan, B. Twamley, E. Salvadori, Y.-K. Liao, M. Chiesa, M. O. Senge, F. Totti, L. Sorace and R. Sessoli, A Heterometallic Porphyrin Dimer as a Potential Quantum Gate: Magneto-Structural Correlations and Spin Coherence Properties, *Angew. Chem., Int. Ed.*, 2023, **62**, e202312936.
57. K. Yamaguchi, Y. Takahara and T. Fueno, *Ab-Initio Molecular Orbital Studies of Structure Reactivity of Transition Metal-OXO Compounds*, 1986.
58. M. Hakimi, H. Rezaei, K. Moeini, Z. Mardani, V. Eigner and M. Dušek, Formation of a copper–copper bond in coordination of a cyclotriphosphazene ligand toward Cu(II): Structural, spectral and docking studies, *J. Mol. Struct.*, 2020, **1207**, 127804.
59. M. Zhang, J. Ming, W. Zhang, J. Xie, P. Lin, X. Song, X. Chen, X. Wang and B. Zhou, Porous Organic Polymer-Derived Fe_2P@N,P-Codoped Porous Carbon as Efficient Electrocatalysts for pH Universal ORR, *ACS Omega*, 2020, **5**, 7225-7234.
60. B. Chen, M. Dong, S. Liu, Z. Xie, J. Yang, S. Li, Y. Wang, J. Du, H. Liu and B. Han, CO_2 Hydrogenation to Formate Catalyzed by Ru Coordinated with a N,P-Containing Polymer, *ACS Catal.*, 2020, **10**, 8557-8566.
61. B. Li, X. Chen, P. Hu, A. Kirchon, Y.-M. Zhao, J. Pang, T. Zhang and H.-C. Zhou, Facile Fabrication of a Multifunctional Metal–Organic Framework-based Sensor Exhibiting Exclusive Solvochromic Behaviors toward Ketone Molecules, *ACS Appl. Mater. Interfaces*, 2019, **11**, 8227-8233.
62. A. J. Elias, P. Mishra, M. S. Kumar, N. Behera and N. Reddy, Reactions of Trialkylamines with the Cyclocarbaphosphazene Cl_2PN $(ClCN)_2$: Selectivity in the Cleavage of Alkyl Groups, *Phosphorus, Sulfur, and Silicon and the Related Elements*, 2005, **180**, 1785-1794.
63. M. Pinsky and D. Avnir, Continuous Symmetry Measures. 5. The Classical Polyhedra, *Inorg. Chem.*, 1998, **37**, 5575-5582.
64. C. Benelli and D. Gatteschi, *Introduction to molecular magnetism: From transition metals to lanthanides*, John Wiley & Sons, 2015.
65. N. F. Chilton, R. P. Anderson, L. D. Turner, A. Soncini and K. S. Murray, PHI: A powerful new program for the analysis of anisotropic monomeric and exchange-coupled polynuclear d- and f-block complexes, *J. Comput. Chem.*, 2013, **34**, 1164-1175.
66. C. Dekker, A. Arts, H. De Wijn, A. Van Duyneveldt and J. Mydosh, Activated dynamics in a two-dimensional Ising spin glass: Rb 2 Cu 1− x Co x F 4, *Phys. Rev. B*, 1989, **40**, 11243.
67. K. S. Cole and R. H. Cole, Dispersion and absorption in dielectrics I. Alternating current characteristics, *J. Chem. Phys.*, 1941, **9**, 341-351.

68. F.-S. Guo, B. M. Day, Y.-C. Chen, M.-L. Tong, A. Mansikkamäki and R. A. Layfield, Magnetic hysteresis up to 80 kelvin in a dysprosium metallocene single-molecule magnet, *Science*, 2018, **362**, 1400-1403.
69. K. R. McClain, C. A. Gould, K. Chakarawet, S. J. Teat, T. J. Groshens, J. R. Long and B. G. Harvey, High-temperature magnetic blocking and magneto-structural correlations in a series of dysprosium (III) metallocenium single-molecule magnets, *Chem. Sci.*, 2018, **9**, 8492-8503.
70. C. A. Goodwin, F. Ortu, D. Reta, N. F. Chilton and D. P. Mills, Molecular magnetic hysteresis at 60 kelvin in dysprosocenium, *Nature*, 2017, **548**, 439-442.
71. A. H. Vincent, Y. L. Whyatt, N. F. Chilton and J. R. Long, Strong Axiality in a dysprosium (III) bis (borolide) complex leads to magnetic blocking at 65 K, *J. Am. Chem. Soc.*, 2023, **145**, 1572-1579.
72. C. A. Mattei, V. Montigaud, F. Gendron, S. Denis-Quanquin, V. Dorcet, N. Giraud, F. Riobé, G. Argouarch, O. Maury and B. Le Guennic, Solid-state versus solution investigation of a luminescent chiral BINOL-derived bisphosphate single-molecule magnet, *Inorg. Chem. Front.*, 2021, **8**, 947-962.
73. C. A. Mattei, V. Montigaud, V. Dorcet, F. Riobé, G. Argouarch, O. Maury, B. Le Guennic, O. Cador, C. Lalli and F. Pointillart, Luminescent dysprosium single-molecule magnets made from designed chiral BINOL-derived bisphosphate ligands, *Inorg. Chem. Front.*, 2021, **8**, 963-976.
74. M. Feng, F. Pointillart, B. Lefeuvre, V. Dorcet, S. Golhen, O. Cador and L. Ouahab, Multiple single-molecule magnet behaviors in dysprosium dinuclear complexes involving a multiple functionalized tetrathiafulvalene-based ligand, *Inorg. Chem.*, 2015, **54**, 4021-4028.
75. O. Galangau, V. Montigaud, J. F. Gonzalez, B. Lefeuvre, V. Dorcet, B. Le Guennic, O. Cador, L. Ouahab and F. Pointillart, N3O6 versus N2O6 coordinated dysprosium slow magnetic relaxation in a tetrathiafulvalene-based dinuclear complex, *Polyhedron*, 2019, **168**, 28-36.
76. B. Lefeuvre, O. Galangau, J. F. Gonzalez, V. Montigaud, V. Dorcet, L. Ouahab, B. Le Guennic, O. Cador and F. Pointillart, Field-Induced Dysprosium Single-Molecule Magnet Based on a Redox-Active Fused 1, 10-Phenanthroline-Tetrathiafulvalene-1, 10-Phenanthroline Bridging Triad, *Front. Chem.*, 2018, **6**, 552.
77. L. F. Chibotaru, Intermolecular mechanism for multiple maxima in molecular dynamic susceptibility, *Phys. Rev. B*, 2018, **98**, 174418.
78. M. Kiskin, E. Zorina-Tikhonova, S. Kolotilov, A. Goloveshkin, G. Romanenko, N. Efimov and I. Eremenko, Synthesis, Structure, and Magnetic Properties of a Family of Complexes Containing a $\{Co^{II}_2Dy^{III}\}$ Pivalate Core and a Pentanuclear $Co^{II}_4Dy^{III}$ Derivative, *Eur. J. Inorg. Chem.*, 2018, **2018**, 1356-1366.
79. L. F. Chibotaru, Multiple relaxation times in single-molecule magnets, *Phys. Rev. B*, 2016, **94**, 104422.
80. J. D. Rinehart and J. R. Long, Exploiting single-ion anisotropy in the design of f-element single-molecule magnets, *Chem. Sci.*, 2011, **2**, 2078-2085.
81. D. Aravena and E. Ruiz, Shedding light on the single-molecule magnet behavior of mononuclear DyIII complexes, *Inorg. Chem.*, 2013, **52**, 13770-13778.
82. D. Shao, W.-J. Tang, Z. Ruan, X. Yang, L. Shi, X.-Q. Wei, Z. Tian, K. Kumari and S. K. Singh, Water-driven reversible switching of single-ion magnetism and proton conduction in a dysprosium sulfonate, *Inorg. Chem. Front.*, 2022, **9**, 6147-6157.
83. C. Das, A. Upadhyay, S. Vaidya, S. K. Singh, G. Rajaraman and M. Shanmugam, Origin of SMM behaviour in an asymmetric Er (III) Schiff base complex: a combined experimental and theoretical study, *Chem. Commun.*, 2015, **51**, 6137-6140.
84. S. K. Singh, T. Gupta and G. Rajaraman, Magnetic anisotropy and mechanism of magnetic relaxation in Er (III) single-ion magnets, *Inorg. Chem.*, 2014, **53**, 10835-10845.

85. T. G. Ashebr, L. La Droitte, X.-L. Li, C. Zhao, J. Wu, Q. Zhou, O. Cador, B. Le Guennic and J. Tang, Edaravone-Based Mononuclear Dysprosium (III) Single-Molecule Magnets, *Cryst. Growth Des.*, 2022, **22**, 5063-5070.
86. L. Zhu, Y. Dong, B. Yin, P. Ma and D. Li, Improving the single-molecule magnet properties of two pentagonal bipyramidal Dy 3+ compounds by the introduction of both electron-withdrawing and-donating groups, *Dalton Trans.*, 2021, **50**, 12607-12618.
87. Y.-C. Chen, J.-L. Liu, L. Ungur, J. Liu, Q.-W. Li, L.-F. Wang, Z.-P. Ni, L. F. Chibotaru, X.-M. Chen and M.-L. Tong, Symmetry-supported magnetic blocking at 20 K in pentagonal bipyramidal Dy (III) single-ion magnets, *J. Am. Chem. Soc.*, 2016, **138**, 2829-2837.
88. J. Liu, Y.-C. Chen, J.-L. Liu, V. Vieru, L. Ungur, J.-H. Jia, L. F. Chibotaru, Y. Lan, W. Wernsdorfer and S. Gao, A stable pentagonal bipyramidal Dy (III) single-ion magnet with a record magnetization reversal barrier over 1000 K, *J. Am. Chem. Soc.*, 2016, **138**, 5441-5450.
89. A. B. Canaj, S. Dey, E. R. Martí, C. Wilson, G. Rajaraman and M. Murrie, Insight into D6h Symmetry: Targeting Strong Axiality in Stable Dysprosium (III) Hexagonal Bipyramidal Single-Ion Magnets, *Angew. Chem., Int. Ed.*, 2019, **58**, 14146-14151.
90. M. Gregson, N. F. Chilton, A.-M. Ariciu, F. Tuna, I. F. Crowe, W. Lewis, A. J. Blake, D. Collison, E. J. McInnes and R. E. Winpenny, A monometallic lanthanide bis (methanediide) single molecule magnet with a large energy barrier and complex spin relaxation behaviour, *Chem. Sci.*, 2016, **7**, 155-165.
91. S. K. Gupta, T. Rajeshkumar, G. Rajaraman and R. Murugavel, An air-stable Dy(iii) single-ion magnet with high anisotropy barrier and blocking temperature, *Chem. Sci.*, 2016, **7**, 5181-5191.
92. Y.-S. Meng, C.-H. Wang, Y.-Q. Zhang, X.-B. Leng, B.-W. Wang, Y.-F. Chen and S. Gao, (Boratabenzene)(cyclooctatetraenyl) lanthanide complexes: a new type of organometallic single-ion magnet, *Inorg. Chem. Front.*, 2016, **3**, 828-835.
93. S.-M. Chen, J. Xiong, Y.-Q. Zhang, Q. Yuan, B.-W. Wang and S. Gao, A soft phosphorus atom to "harden" an erbium (III) single-ion magnet, *Chem. Sci.*, 2018, **9**, 7540-7545.
94. P. B. Jin, K. X. Yu, Q. C. Luo, Y. Y. Liu, Y. Q. Zhai and Y. Z. Zheng, Tetraanionic arachno-Carboranyl Ligand Imparts Strong Axiality to Terbium (III) Single-Molecule Magnets, *Angew. Chem., Int. Ed.*, 2022, **61**, e202203285.
95. C. A. Goodwin, D. Reta, F. Ortu, J. Liu, N. F. Chilton and D. P. Mills, Terbocenium: completing a heavy lanthanide metallocenium cation family with an alternative anion abstraction strategy, *Chem. Commun.*, 2018, **54**, 9182-9185.
96. T. P. Latendresse, V. Vieru, B. O. Wilkins, N. S. Bhuvanesh, L. F. Chibotaru and M. Nippe, Magnetic Properties of a Terbium–[1]Ferrocenophane Complex: Analogies between Lanthanide–Ferrocenophane and Lanthanide–Bis-phthalocyanine Complexes, *Angew. Chem., Int. Ed.*, 2018, **57**, 8164-8169.
97. S. K. Singh, N. K. Tibrewal and G. Rajaraman, Density functional studies on dinuclear {$Ni^{II}Gd^{III}$} and trinuclear {$Ni^{II}GdI^{II}Ni^{II}$} complexes: magnetic exchange and magneto-structural maps, *Dalton Trans.*, 2011, **40**, 10897-10906.
98. T. Rajeshkumar, S. K. Singh and G. Rajaraman, A computational perspective on magnetic coupling, magneto-structural correlations and magneto-caloric effect of a ferromagnetically coupled {Gd^{III}–Gd^{III}} Pair, *Polyhedron*, 2013, **52**, 1299-1305.
99. T. Rajeshkumar, H. V. Annadata, M. Evangelisti, S. K. Langley, N. F. Chilton, K. S. Murray and G. Rajaraman, Theoretical Studies on Polynuclear {CuII5GdIII n} Clusters (n= 4, 2): Towards Understanding Their Large Magnetocaloric Effect, *Inorg. Chem.*, 2015, **54**, 1661-1670.
100. E. Cremades, S. Gomez-Coca, D. Aravena, S. Alvarez and E. Ruiz, Theoretical study of exchange coupling in 3d-Gd complexes: Large magnetocaloric effect systems, *J. Am. Chem. Soc.*, 2012, **134**, 10532-10542.